Modelling of the buckling of a diaphragm–spine structure for a wave energy converter

K M Collins[1*], M Meng[2], H R Le[2], D Greaves[1], N. W. Bellamy[3]
[1]School of Marine Science & Engineering, Faculty of Technology, Plymouth University,
Drake Circus, Plymouth, Devon, England, PL4 8AA, UK
[2]Department of Mechanical Engineering and Built Environment, University of Derby, Markeaton Street, DE22 3AW, UK
[3]Sea Energy Associates Ltd, Ergo House, Mere Way, Ruddington Fields, NG11 6JS Ruddington, UK
[*]E-mail: keri.collins@plymouth.ac.uk

Abstract
A wide range of wave energy converter (WEC) designs exists, and the SeaWave WEC uses an unstable buckled spine mode of operation. The SeaWave consists of a hose and buckled spine-diaphragm, which pumps air along the device under wave action. A physical model and finite element analysis (FEA) is compared to a previous theoretical model in this paper. The FE model was developed in ABAQUS 6.14 using shell, solid and contact elements and the analysis was done with a quasi-static approach to reduce the computational costs. The physical model was a scale version of the novel arrangement of the spine and diaphragm made from steel, polycarbonate and latex rubber. Geometry of the deformed device was investigated results showed an increase in transverse and longitudinal curvature as the compression rate increased. The FEA tended to overestimate the bending stiffness of the model, and hence the transverse curvature, because certain behaviours of the physical model were not captured. The force required to switch from one buckled state to another was measured both in the physical and FEA models and the potential energy storage was estimated to be 0.5 J/m of device at a compression rate of 0.1%.

Keywords: Buckling, snap-through force, finite element analysis, Wave energy converter, deformable structure, diaphragm

This article has been published in Materials & Design vol. 119, 2017. The article can be found on the publisher's website along with supplementary material: http://dx.doi.org/10.1016/j.matdes.2017.01.041.

1 Introduction

The wave energy industry lags behind the tidal energy industry in terms of technology convergence and readiness [1] and there are many different devices currently being developed. Wave energy converters (WECs) may be categorised by their operating principle, typically an oscillating body WEC will comprise parts moving relative to one another. The moving parts will translate the wave motion to the device machinery and either use such a motion to mechanically drive an on-board power take-off or use the motion to do work on a fluid, which can then be dealt with on shore. A comprehensive description of the different types of WEC is found on the EMEC website[1] and a review of the many different types of WEC and their necessary power equipment has been carried out by [2]. One of the difficulties facing the WEC industry is the number of concepts in development; the lack of design convergence has led to a large range of devices spanning concept designs to working prototypes. With no clear market leader in WEC technology, new designs are constantly being developed.

One such WEC is the SeaWave, a hose and spine attenuator-type device. The development of any new WEC is a multi-stage process and the aims and objectives of the development step progress with each of the stages. The SeaWave model described in this paper is a width-wise 1:10 scale model in its validation phase [3].

The two main elements of the SeaWave design are the post-buckled spine and the diaphragm-hose enclosure, Figure 1. When buckled, the spine stores elastic energy that is transferred to the working fluid under wave action and so the mechanical characteristics of the spine are directly linked to the performance of the WEC. The hose entrains the working fluid, allowing it to be pumped along the device as the buckled spine oscillates. As long as the waves have a prevailing direction, the air pumping of the device will be in the up-wave to the down-wave direction. It is envisaged that the air will drive a turbine at the exhaust end of the device to transform the wave energy into electricity; however this is out of the scope of the current work. The device uses the unstable nature of the buckled spine as the mechanism for pumping.

1.1 *The SeaWave as a hydrostat*

The natural world is full of anisotropy in its structural elements [4] and hydrostats, which take their shape and stiffness from internal fluid pressure, are being investigated as a way to induce controllable anisotropy in composite materials [5]. FEA can also be used to investigate large deformations in anisotropic elastic materials [6]. The current design of the SeaWave has longitudinal and transverse stiffening elements resisting the compression of the buckled spine (see Section 3.1 for more details). If considered as a hydrostatic device, this arrangement allows the SeaWave to resist elongation and shortening but leaves it open to kinking. In contrast hydrostats with helical-

[1] http://www.emec.org.uk/marine-energy/wave-devices/

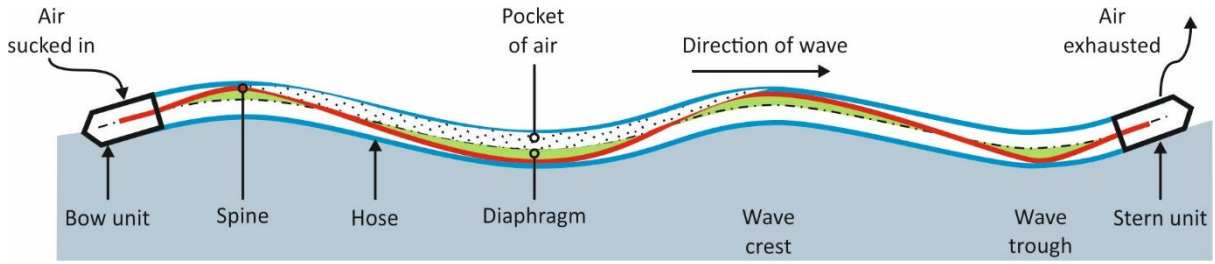

Figure 1 – Working principle of the SeaWave device under wave action.[10]

crossed stiffening fibres are able to bend smoothly while restricting twisting around the long axis [7, 8]. Preliminary experiments with a full sectional model (see for example [9]) revealed that the deformation of the device under wave action was very sensitive to the air pressure inside the model. This can be attributed in part to the longitudinal and transverse stiffening elements present in the design.

1.2 Buckling and bistability

Buckling is the out-of-plane deformation of a structure that has reached an elastic instability thanks to an in-plane compression [11]. Once buckled, a structure may exhibit several stable states, often symmetric, which represent minimum energy geometries.

Energy harvesting using bistable mechanisms has been investigated extensively but only at small scales. The recent trends and advances in buckled beams for smart structures have been discussed and the authors define two main disciplines: energy related and motion related applications [12]. Using the concept map of buckling-induced applications [12], the SeaWave falls into the hybrid form category since it is represents a prototype of a structure designed for bistability.

1.2.1 Buckling forces

In recent years, much research has been carried out on the buckling properties and energy use of beams, however this has been confined to the micro-machine regime. The relationship between the force and displacement is non-linear for buckled and post-buckled beams [13, 14, 15]. A variety of numerical methods are used to solve for loads and deformed configurations such as shooting methods based on boundary value problems [16, 17], incremental displacement methods [14] or non-linear or large deformation FEA [13, 18, 19, 20, 21]. Hao and Mullins [21] note that displacement control is necessary in the set-up of the FEA model since the force is no longer a suitable control parameter in the negative stiffness range, which occurs between the critical buckling load and the location of maximum snap through force magnitude.

The maximum force needed to snap from one stable state to another was derived by Vangbo [22] for a clamped-clamped beam and he concluded that by taking into account the contraction of the beam, the maximum snap-through force and the activation energy were both lower. Additionally, snap-through behaviour has been found to be asymmetric if the beams are hinged [13, 18]. The location of force application was investigated in relation to snap-through [23] and showed that shifted actuation could decrease or increase the activation energy depending on the geometry considered.

1.2.2 Energy harvesting

Research on the use of elastic instability has increased over the last decade and energy production forms a large part of this research [12] though this also tends to be at the micro-scale. A typical method to harvest energy is using piezo electric components, for which an applied mechanical strain will generate an electric charge in the component and vice versa. It has been noted that a large portion of research into vibration harvesting considers vibrations with a frequency greater than 60 Hz possibly because the conversion to electricity is more efficient [24]. Harvesting of low frequency (<10 Hz) vibrations has been investigated and in many cases [24, 25, 26] the bistable mechanism is used to induce a mechanical up conversion of the frequency of vibration.

Despite a similarity in input frequencies (gravity and infra-gravity sea waves have frequencies in the range of 0.01 Hz to 1.00 Hz, the working principle of the SeaWave is not to up-convert mechanical vibrations to drive piezoelectric components. Rather, the induced wave motion is used to induce the snap-through as a method of pumping air.

1.3 Previous work

In our previous work [10], a first-order mathematical model of the spine and diaphragm was developed to describe the geometry of the deformed physical model and this is reviewed in Section 2. The theory was based on two components – the spine and the diaphragm and predicted the average spine curvature and the diaphragm bending correctly. However, the theory did not include stiffener that is essential for connecting the air chamber and it could not predict the 3D shape of the diaphragm. The force required to snap through the diaphragm was also not attempted due to the complexity of the structure. Here, the work is extended to develop a FEA model of the spine, diaphragm and side stiffeners in order to investigate the deformed geometry and the snap-through force of the buckled device. It is hoped that by having a more sophisticated representation of the physical model, the response of the complex structure to external load may be assessed. Future work on the numerical model will attempt to couple the hydrodynamics with the structural dynamics in order to understand the response of the structure in waves.

The SeaWave concept has a complex working mechanism and it is too early in its development stage to assess its functioning as a whole. Our paper focusses on the spine and diaphragm sections only to investigate the behaviour of these elements. There are two principal questions to be answered in this paper. Can an FE model be used to represent the 3D geometry of the buckled spine, and if so, can it be used to assess the loads needed to drive the device? To do this, Section 2 summarises the theoretical model of the simplified physical model. The FEA and physical model experiments are described in Section 3, with results presented in Section 4. The results are discussed in terms of the bending geometry and the deformation force of the models in Section 5 and conclusions are drawn in Section 6.

2 Theoretical model

The previous paper by the authors [3] developed a simplified model to investigate the longitudinal curvature, curvature in the *x*-*y* plane as defined in Figure 2 and the transverse deflection (in *x*-direction) of the diaphragm using the minimum energy principle. The transverse deflection *h* and the longitudinal radius of curvature *R* can be derived as:

$$\boldsymbol{h} = \sqrt{\boldsymbol{C}\frac{\Delta \boldsymbol{L}}{\boldsymbol{L_0}}} \quad (1)$$

$$\boldsymbol{R} = \sqrt{\boldsymbol{C}\frac{\boldsymbol{L_0}}{\Delta \boldsymbol{L}}} \quad (2)$$

The quantity $\Delta L/L_0$ is the compression rate of spine given by the change in length along the *y*-axis, ΔL, divided by the original length, L_0, and the constant, *C*, is given by:

$$\boldsymbol{C} = \boldsymbol{hR} = \sqrt{\frac{\boldsymbol{E_2 B_2 {t_2}^3 {B_1}^3}}{\boldsymbol{24 \alpha E_1 {t_1}^3}}} \quad (3)$$

In which t_1, is the thickness of single diaphragm sheet; t_2, the thickness of spine; B_1, the undeformed width (in *z*-direction) of the diaphragm; B_2, the width of the spine; α, the factor of end conditions in three-point bending; E_1, the elastic modulus of diaphragm and E_2, the elastic modulus of spine. The transverse displacement, *h*, is shown to the edge of the diaphragm in Figure 2 but in the physical model described in Section 3.1, the side stiffener was the lateral extent.

Accurately modelling the boundary conditions of the theoretical model was difficult. The factor of end-conditions, α, was introduced to account for the different types of end. In the theoretical model, α functioned as a fitting parameter that allowed the model to be tuned to the experimental conditions.

The theoretical predictions of transverse deflection and longitudinal radius of curvature were in good agreement with measurements taken on a small scale diaphragm structure consisting of a plastic spine and sectioned diaphragm with restraining nylon string on the edges of the diaphragm. However, the model did not account for the effect of stiffeners, which are required for the attachment of the air chambers and the fins in the final system. The finite element model described in Section 3.2 includes the effect of stiffeners on both sides of the diaphragm and includes more sophisticated boundary conditions than those of the theoretical model. The FE model will be compared with the theoretical model of our previous work and the experimental data presented here.

3 Materials and methods

Following previous work [10] in which the diaphragm design was described, scale models of the proposed device were constructed: a second-stage sectional model of the SeaWave was constructed that omitted the hose and a larger model that included all elements, which was used to test the operating concept (not further discussed here).

The sectional model was a flat, layered construction, replicating the components inside the hose: the spine, the diaphragm and hinges and the latex cover; as well as the side stiffeners that were outside the hose on the larger model. These elements were recreated in the FEA model

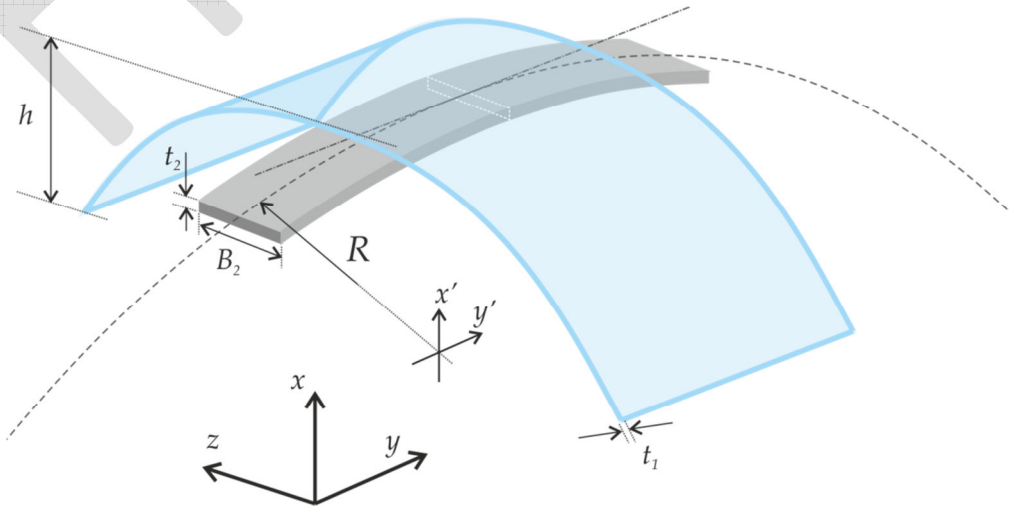

Figure 2 – Sketch of the model showing the definition of the curvature in two planes. Note that the diaphragm section curvature does not necessarily describe a semi-ellipse.

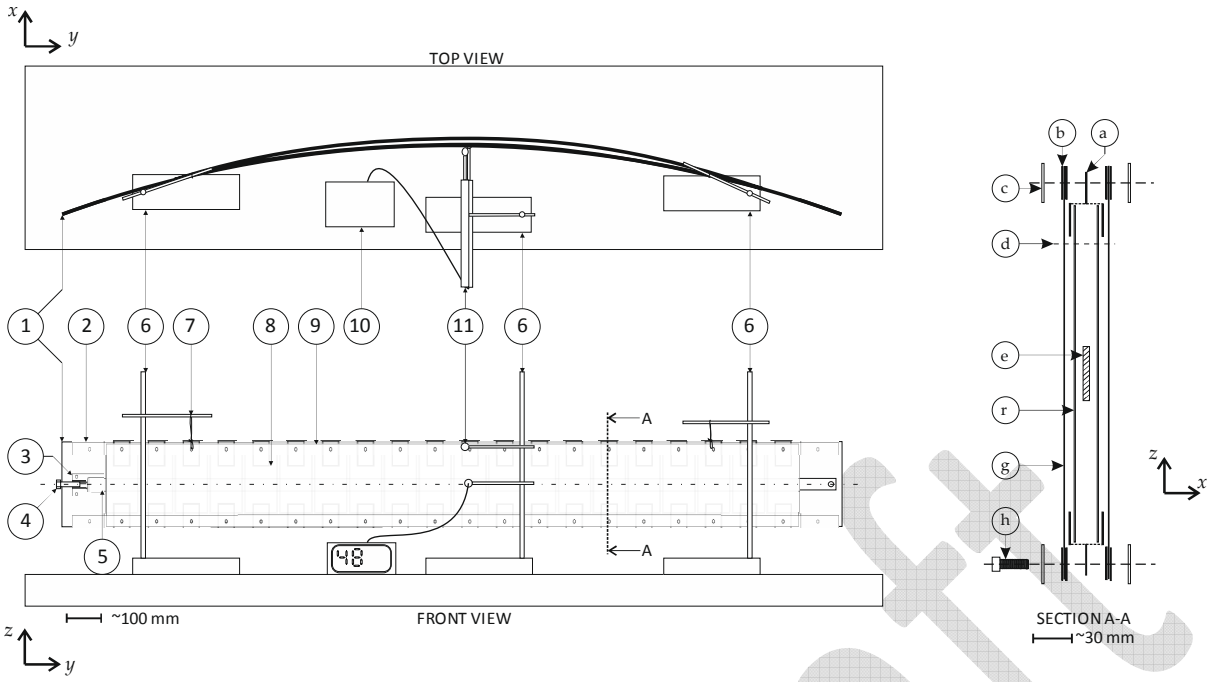

Figure 3 - Setup for experimental measurements and zoomed in sectional view of the relative placement of the layers in the experimental model with elements shown approximately to scale. (h) M4 assembly bolt, (g) latex sheet, (f) PC diaphragm section, (e) EN43 steel spine, (d) approximate limit of bond between PC diaphragm sections, (c) PC side stiffeners, (b) glass-fibre cross-weave tape edging on latex, (a) glass-fibre cross-weave tape hinge.

with physical properties chosen to best model the anisotropy of the overall structure.

3.1 Physical model testing

The layers of the model are shown in Figure 3 and letters in parentheses refer to the part designation in the diagram. The model spine (e) was made from 2.0 mm x 30 mm x 2200 mm EN43 spring steel (Milton Keynes Metal) housed between two sheets (f) of 0.75 mm x 100 mm x 250 mm polycarbonate (Lexan 9030) that had been bonded together at each end using a single component solvent based cement (Extrufix, BOSTICK). The bonded section on each side of the polycarbonate layer measured 100 mm by approximately 50 mm (d). Once bonded, the polycarbonate sections were left to cure for several days and no debonding was witnessed. So that the polycarbonate sections were free to rotate in the model, glass-fibre cross-filament tape (a) (Tesa 4579) was stuck to each side of the bonded polycarbonate sheet with a 50 mm over-hang. The over-hang was stuck to itself to create a tab to be used as a hinge and a hole was manually pierced in the tape hinge at a specified point.

A 0.2 mm thick, 305 mm wide latex sheet (g) was fixed in place on either side (top and bottom) of the polycarbonate sections and this sheet ran the whole length of the model. The latex was attached to the polycarbonate sheets at several points along the models using double-sided tape (Tesa 56172). The long edges of the latex were bound in glass-fibre cross-filament tape (b) (Tesa 4579) to minimise stretching of the latex and to prevent tear propagation at the bolt holes. Holes were pierced or drilled through the cross-filament tape and latex, at 102 mm intervals. These holes corresponded to the holes cut in the tape hinges on the polycarbonate sheets, so that there were 2 mm of clearance between each of the polycarbonate sections in the assembled model.

A 0.75 mm thick, 30 mm wide polycarbonate (Lexan 9030) stiffening strip (c) was placed on the top and bottom of the latex on the model and holes 102 mm apart along the centreline of the stiffeners allowed the model to be bolted together. In total, 20 polycarbonate diaphragm sections composed the model and these were numbered 1 – 20 starting at the compression bolt (4) end.

3.1.1 Experimental setup

Two anodised steel plates were put on the ends of the model in an attempt replicate the boundary conditions of the finite element model. Figure 3 shows the components of the model (1) and the arrangement of the equipment. At one end, the spine (5) was bolted to the steel plate (2). At the other end, the spine entered a slot in a polycarbonate end piece (3) that was bolted to the end. The polycarbonate end piece had a tapped hole in one end to allow a bolt (4) to be introduced that would contact the spine and compress it as the bolt travelled along the slot. The PC side stiffeners (9) on the model were bolted to the end plates.

The model was suspended from wires (7) looped around the bolts on sections (e.g. 8) numbered 3 and 18 that were in turn suspended from two retort stands (6). The uprights of the retort stands contacted the model on the inside of the curve when the model was deformed.

3.1.2 Test conditions

Experiments were conducted in three parts. First to measure *h*, the transverse distance between the edge and

the centre of the model, the model was set up as shown in Figure 3. Two linear displacement gauges (11) were set up in front of the model in line with the middle of the central section: one at the height of the longitudinal centreline, and one at the top edge. The sensor at the top edge was displaced horizontally so that the sensor head made contact with the model and not the bolt and this displacement was less than 5 mm. Voltage readings were taken from the transducer display box (10) attached to each sensor and converted to distance measurements after the experiment was concluded.

In the second experimental set-up, the two displacement sensors were replaced with a large ruler (length, L_r) positioned at the longitudinal centreline. A smaller rule was used to measure the distance between the metre rule and the model surface, D, Figure 4, so that the longitudinal curvature, R, could be calculated using Equations 4 – 6.

$$H = \sqrt{D^2 + \left(\frac{L_r}{2}\right)^2} \quad (4)$$

$$\theta = \tan^{-1}\left(\frac{L_r}{2D}\right) \quad (5)$$

$$R = \frac{H}{2}cos(\theta) \quad (6)$$

For the geometry-measuring experiments, the strain on the spine was increased by successive turns of the bolt. The bolt used to compress the spine had a pitch of 1 mm meaning that for every full turn of the bolt, the travel, d, was equal to 1 mm. Uncertainty in the compression measurement was due to uncertainty of the initial contact of the bolt (labelled (4) in Figure 3) and the end of the spine at the beginning of each experiment. To facilitate the recording of the number of turns made, a large piece of polycarbonate, which had a reference line marked on it, was attached to the head of the bolt. Measurements of transverse deflections were taken for a number of loading and unloading cycles and the mean and 95% confidence intervals were calculated. The measurement of the longitudinal radius of curvature, R, was only completed on the final loading of the model.

The snap-through force was measured by loading a mass hanger that was attached to the spine at the model's longitudinal centre (section 11) via a cord running over a pulley and attached to the spine by a strong magnet. At a given spine compression (number of bolt turns), the mass hanger was progressively loaded until the snap through motion of the model was observed. This was repeated to give three or four measures at each strain value and then the strain was increased. Seven values of strain were chosen spanning the range used in the geometry experiments.

3.2 FEA simulation

A three-dimensional nonlinear finite element model was constructed using ABAQUS 6.14 commercial finite element code. If in the FE model, the diaphragm were constructed as a series of discrete sections, it was expected that the connections between sections would cause the computation time to be prohibitively long. To remedy this, the diaphragm was modelled as one orthotropic body made of two shells bonded together. The spine core was modelled as an isotropic body sitting in the central cavity of the diaphragm. The stiffeners were modelled as long and narrow shells bonded to the diaphragms at the edges.

The definition of the boundary conditions was critical to achievement of the desired numerical description. The schematic of the boundary conditions are illustrated in Figure 5 with a hinge condition imposed at one end of the structure and at the opposite end a MPC (multi-point constraints, i.e. both spine and diaphragm are bonded to an imaginary rigid body) boundary condition that allowed movement in the in-plane direction (i.e. y-direction) was applied. The spine compression was defined as a displacement from the hinged end of the diaphragm along y, causing the diaphragm to buckle in the longitudinal and transverse directions simultaneously. Owing to the magnitude of the buckling, a large displacement algorithm

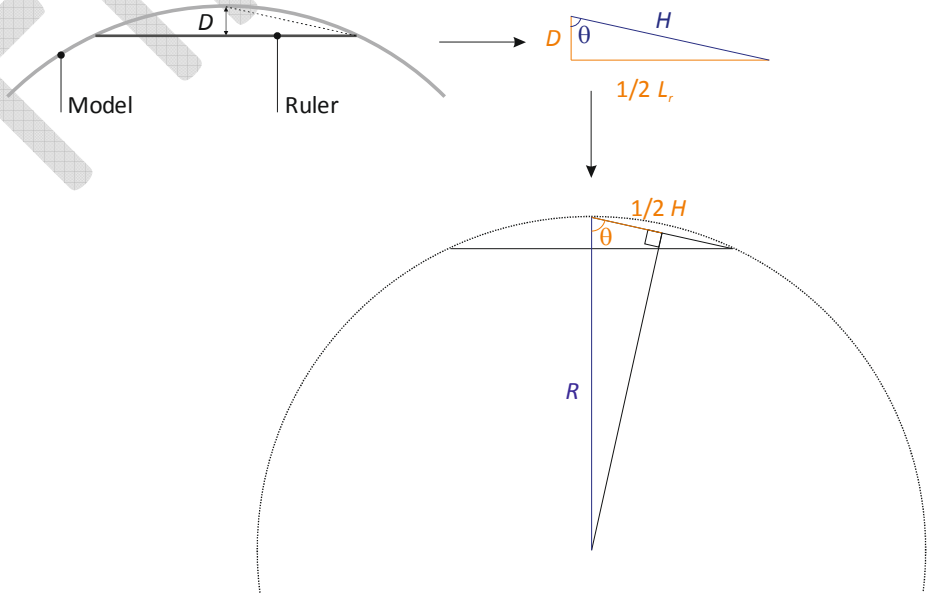

Figure 4 – Schematic showing the method of calculation for the longitudinal curvature.

Table 1 – Material properties of the diaphragm and spine structure, subscript values 1,2 and 3 refer to the *x*-, *y*- and *z*-axis respectively, corresponding to the model thickness and the longitudinal and transverse directions.

SPINE				DIAPHRAGM			
Property	Symbol	Value	Unit	Property	Symbol	Value	Unit
Modulus	E	200	GPa	Young's modulus	E_1	2.30	GPa
Poisson ratio	ν	0.30		Young's modulus	E_2	20.0	MPa
				Young's modulus	E_3	2.30	GPa
				Poisson's ratio	ν_{12}	0.03	
STIFFENER					ν_{23}	0.03	Poisson's ratio
Property	Symbol	Value	Unit	Poisson's ratio	ν_{13}	0.37	
Modulus	E	2.30	GPa	Shear modulus	G_{12}	83.0	MPa
Poisson ratio	ν	0.37		Shear modulus	G_{23}	83.0	MPa
				Shear modulus	G_{13}	83.0	MPa

with non-linear control was applied.

Simplifications were used in the FEA analysis in order to facilitate numerical implementation. The diaphragm was regarded as bonded to the edge of stiffeners whereas in the physical model it was hinged. The stiffener was modelled as one body to save computational effort but on the physical model it was a sandwich structure of PC elements (refer to Figure 3 for details of the construction). The use of a single piece to model the diaphragm meant that the bending stiffness would be overestimated. It should be noted that geometry was drawn by sweeping the profiles through an arc path with 2 mm initial deflection from the *y*-axis so that the spine could buckle in a designated direction when the compression was applied.

3.2.1 Material properties

The mechanical properties used in the FEA model are as presented in Table 1. The material used for the spine core was structural steel. The physical diaphragm comprised a series of sections made from polycarbonate and all the sections linked by two layers of latex (top and bottom); this was characterized in the finite element model as an orthotropic structure with properties displayed in the Table. Table 1 also shows the material properties of the diaphragm with reference to a geometric coordinate axes where the indices 1, 2 and 3 denote the *x*-, *y*- and *z*-axis respectively. These mechanical characteristics were carefully selected in order to describe the characteristics of the structure. The transverse modulus (in the *z*-direction) and the modulus in the *x*-direction of the diaphragm are determined by the diaphragm material. The longitudinal modulus (*y*-direction) of the diaphragm was in-line with that of the latex used [27]. To induce anisotropy in the model, the Young's modulus in the longitudinal direction, E_2, was reduced from 2.3 GPa to 20 MPa and the Poisson's ratios ν_{12}, ν_{23} were reduced to satisfy the compatibility of the material.

3.2.2 Discretisation

The models were discretized into sufficient number of elements to allow for adequate representation of the deformation for the diaphragm with the spine core and the stiffeners.

All parts are meshed with shell S4R elements of ABAQUS numerical code [28], which has 4-node doubly curved thin or thick shell. Mesh controls were applied to the stiffener and spine for a mesh size of 5 mm and to the diaphragm of 10 mm. The interaction between the spine and the diaphragm was described as surface-surface contact which permitted small sliding using the penalty algorithm as defined within the contact capabilities of the ABAQUS finite element code. The friction coefficient was defined as 0.2 in order to get a convergent solution quickly. The analysis becomes a nonlinear finite element analysis because of the contact between the spine and the diaphragm, this is a common phenomenon in the engineering field because no component of a system can work independently from the other parts.

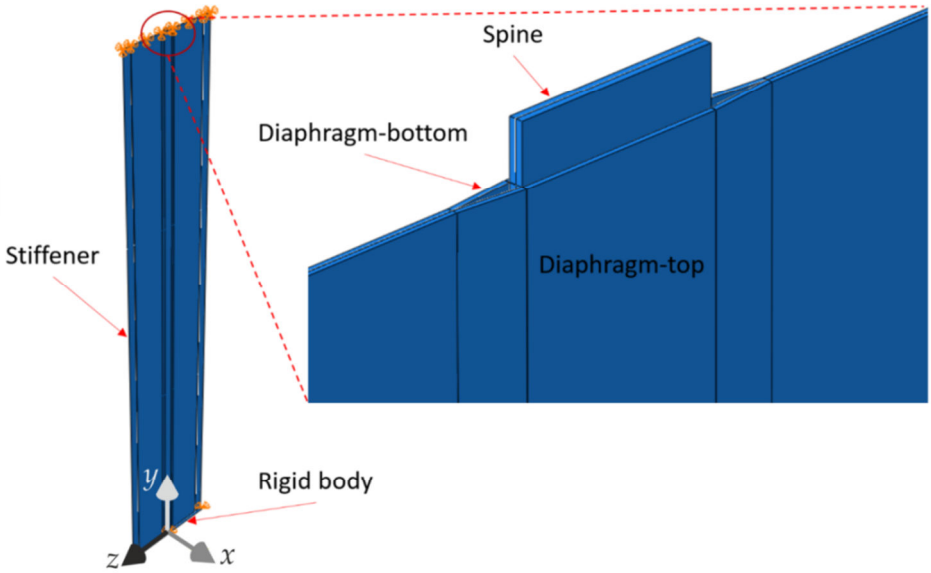

Figure 5 – Schematic of the loading and boundary conditions of the diaphragm/spine assembled structure. The shell element was rendered as 3D solid for the visualisation. A hinge condition was imposed at one end (*y* = 0), allowing rotation around the *z*-axis but no translation. At the other end, movement in the ±*y*-direction was allowed.

3.2.3 Model geometry

In order to study the effect of the stiffener thickness on the behaviour of the diaphragm-spine structure, a parametric study was undertaken in which the thickness of the stiffener was varied. Nominally, the configuration of the FEA model structure was the same as the physical model and the geometrical properties of the components of the finite element models are shown in Table 2. Since in the FEA, the spine is compressed as the diaphragm is effectively in tension, the length of the spine was deliberately made longer than the diaphragm to prevent the spine from retracting into the diaphragm. The values chosen for spine compression, Table 2, were a subset of the range used in the experiments (2 mm – 8 mm) and the spine compression was ramped to help achieve convergence in the model

Table 2 – Geometry of the FEA model components used with stiffeners of 2 mm and 3 mm thick.

SPINE				DIAPHRAGM		
Compression [mm]	Thickness, *t*, [mm]	Length, *l*, [mm]	Width, *w*, [mm]	Thickness, *t*, [mm]	Length, *l*, [mm]	Width, *w*, [mm]
(2, 4, 6, 7, 8)	(2, 3)	2012	30	1.5	2000	290

3.2.4 Extraction of deformation and loading parameters

The vertical displacement of the spine/diaphragm can be extracted from the FEA. To do this, the curves of the displacement along the *y*-axis were fitted with a polynomial equation with the ends of the curve (approximately 10%) ignored to mitigate the end effects. Using the sign convention in Figure 5, an expression for U_1 was obtained. The expression for U_1 was differentiated twice with respect to the node location lengthwise of the spine and the reciprocal of the result obtained from this expression about the centre ($y = 1$) gives the value for the longitudinal curvature, *R*, *i.e.*

$$R = \frac{1}{U_1''} \qquad 7$$

The transverse deflection of the diaphragm, *h*, was calculated as the difference between the position in the *x*-direction of the highest and lowest points of the transverse section along the length of the FEA model. This equated to the maximum displacement of the spine minus the maximum displacement of the stiffener. The transverse deflection is an important parameter which is used for the evaluation of the energy storage.

The stiffness of the structure was evaluated by examining the deformation of the curved spine taken from the previous step. A displacement load was applied to the mid-length of the spine and the reaction force at the loading point was evaluated. The boundary conditions of the model allow rotation but no translation of one end of the model and rotation and translation only along the longitudinal (*y*) axis at the other end.

4 Results

In this section, we consider the results from the physical model in the context of a validation case for the FEA model, in terms of the transverse deflection at the longitudinal centre of the model, the radius of curvature and the snap-through force. The measurement of the transverse deflection of the physical model was limited to one measurement at the longitudinal centre and so the FEA model was used to investigate the deflection along the whole length. Where possible the results are compared with the theory presented in previous work.

4.1 Experimental validation of geometry

In total, twelve sets of measurements were taken for the transverse deflection but these were not always conducted in loading/unloading pairs. There were four such paired cycles and Figure 6 shows only two of these for clarity. The transverse deflection measured on the two loading cycles is the same despite some local variation. The unloading cycles are different: one gives values of *h* lower than on the loading cycle (Exp II U) whereas the other (Exp I U) shows *h* to be the same or higher on the unloading cycle. Given the variation in the results, as discussed in Section 5, it was decided to collate and average the results from the twelve data sets for comparison with the theoretical and numerical analysis.

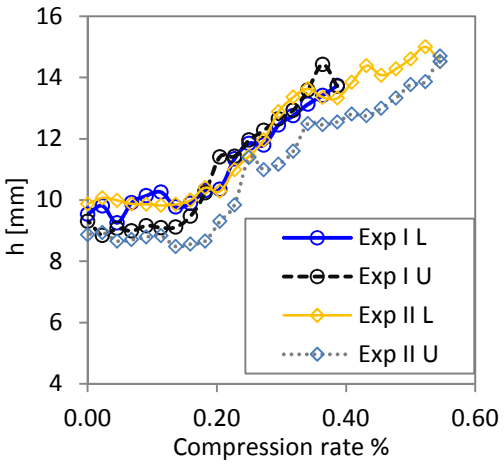

Figure 6 – Loading (L) and unloading (U) of the physical model and the effect on the transverse deflection, *h*.

The transverse deflection, *h*, results of the various analyses conducted are displayed in Figure 7(a). The FEA and the theoretical analysis both show an increase in the transverse deflection as the compression rate increases. The experimental data accord with the trend but also indicate that after a certain point, the deflection plateaus or may even begin to decrease. At compression rates lower than 0.1%, the experimental data indicate a residual curvature of the device of less than 10 mm.

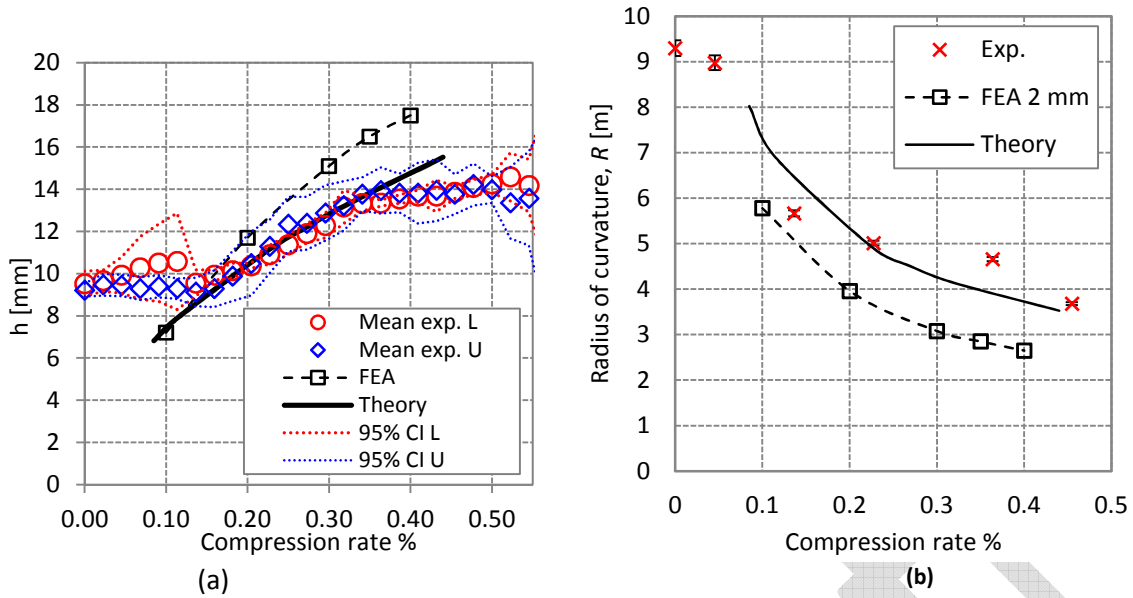

Figure 7 - Comparison of experimental, theoretical and FEA results (stiffener thickness 2 mm), (a) transverse deflection and (b) radius of curvature. For the transverse deflection, the experimental data show vertical error bars showing the 95% confidence interval of up to 6 data. For the radius of curvature, the data represent one experiment only and so error bars indicate the uncertainty in the measurement.

The agreement between the experimental data and the theory is close at compression rates between 0.1% and 0.4%. At low compression rates, the deflection calculated by the FEA agrees well with those found experimentally and from the theory. As the compression rate increases, the deflection calculated by the FEA is larger than predicted by theory by approximately 2 mm, but the rate at which the deflection increases with compression rate slows.

It is noted that the central hole of the diaphragm widened and the end plates deformed when the spine compression was increased further. The assumption of no separation between the spine and the diaphragm and the rigid end plates was no longer valid.

At large compression rates, the difference between the transverse deflection on the loading and unloading cycles is observable. This may not be a statistically significant difference however as very few data were recorded at compression rates above 0.55%. This is indicated by the very large confidence intervals that at their extreme values, off the scale of Figure 7(a), provide a confidence interval for only two data.

Below a compression rate of 0.1%, the radius of curvature and the transverse deflection is almost unchanged in the physical measurements. This is likely owing to the the wrinkling during assembly of the stiffeners, which were made of thin PC plates and glass fibre tape; the initial compression counteracts the wrinkles. Nevertheless, within the operation range 0.1% – 0.5%, the physical measurements have good agreement with the FEA and theoretical analysis.

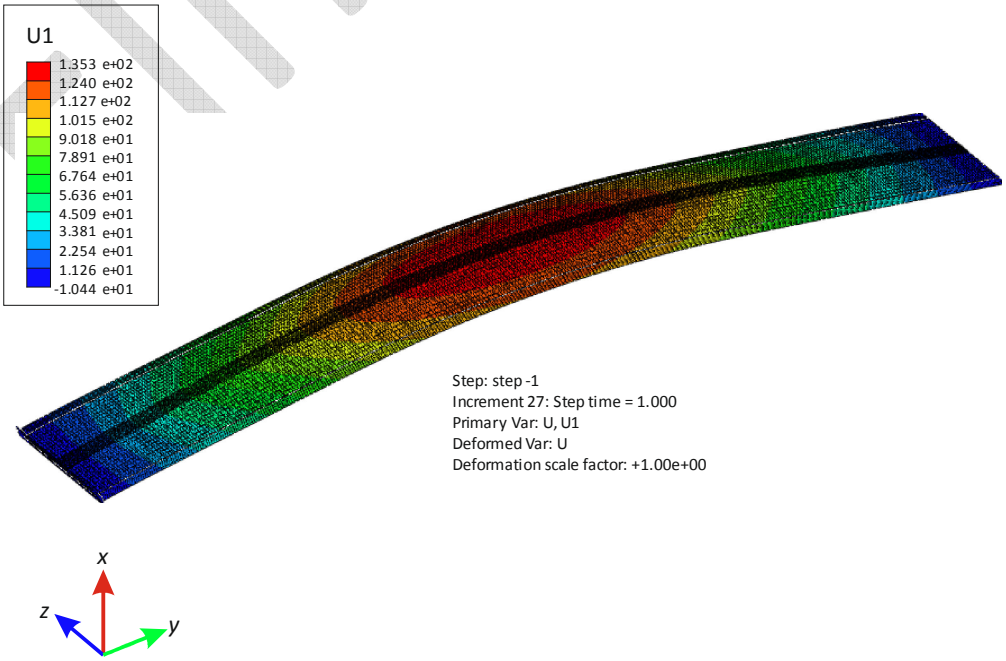

Figure 8 - Deformed shape from FEA for spine compression of 0.35%. U1 represents the deformation in the *x*-direction in millimetres.

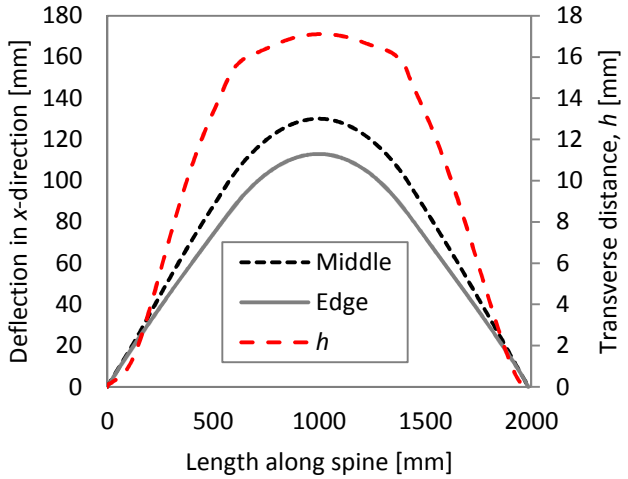

Figure 10 – Representative plot from FEA of diaphragm deflection in the *x*-direction for diaphragm compression rate of 0.35%. The difference between the deflection of the middle and the edge, the transverse deflection, *h*, is also shown.

Figure 7(b) shows the radius of curvature of the spine against compression rate, which decreases for increasing compression. The experimental data match the theory well, although the FEA gives a value approximately 1.5 m below the theory at all values of compression. The experimental data indicate a residual longitudinal curvature on the model of approximately 9.3 m (D = 14 mm). This result was one of the experiments from which the mean h value was calculated (Figure 7(a)) and represents approximately the same value (at zero compression D = 14 mm, h = 9.2 mm and mean h = 9.4 mm).

The longitudinal curvature is sensitive to the input measurements and so error vertical error bars around the experimental data in Figure 7(b) represent an uncertainty of 0.5 mm in both the measurement of D and of the length of the rule (see Figure 4 for details). Whilst this results in an appreciable physical difference in R (±0.17 m at a maximum), over the range of experimental values, it does not seem significant. Uncertainty in the experimental tests will be discussed futher in Section 4.

Figure 8 shows the deformed shape of the diaphragm when a spine compression, d, of 7 mm (compression rate of 0.35%) was applied. The colour bar in Figure 8 indicates the displacement in the x-direction, U_1. The results show that the FEA model deformed longitudinally by about 135 mm with a transverse deformation of approximately 15 mm, as shown in Figure 7(a).

The deformation is quantified along the length of the model in Figure 10, which shows the deflection of the diaphragm along the centreline and at the edge for a model with 2 mm thick side stiffeners. The diaphragm curves in both directions and second-order polynomials have been fitted to the data, which were used in the calculation of the radius of curvature (as described in Section 3.2.4). The difference between the deflection of the middle and the edge, the transverse deflection, h, indicates that there is a central portion of the spine for which there is a smaller transverse curvature, Figure 10.

4.2 Response to external load

A displacement in the x-direction was applied to the deformed structure with an initial spine compression rate. Figure 9 shows the diaphragm deformation, U1, at a compression of about 30 mm – the moment before it buckled and became unstable.

Figure 11 shows how the reaction force changed with the displacement in x at an initial spine compression rate of 0.1%. The reaction force increased almost linearly until the critical point, and then it dropped significantly after a sharp spike corresponding to the shift of the position of the maximum deflection. The maximum force prior to the spike is regarded as the critical load for buckling. The stored energy in the structure can be calculated by integrating the force-displacement curve shown in Figure 11 up to the point of buckling using standard numerical integration methods.

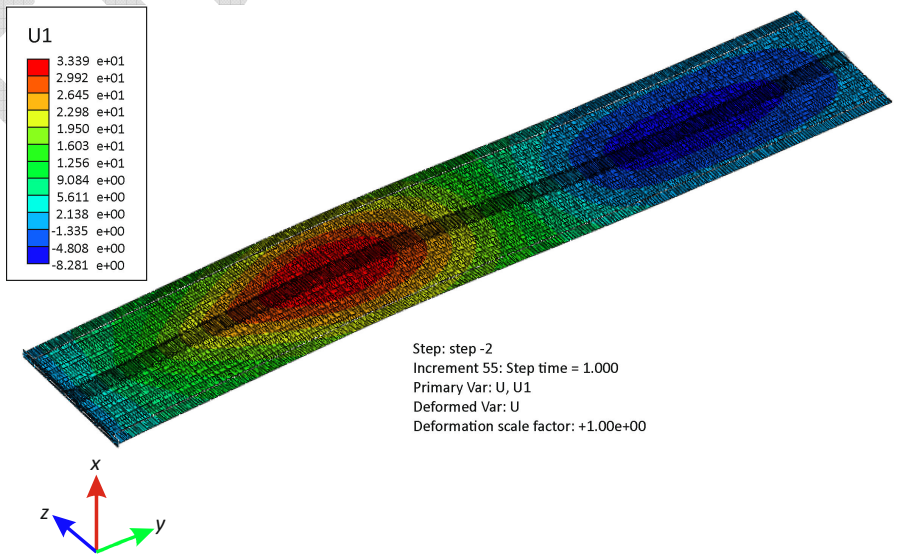

Figure 9 - Deformed structure under central load in –*x*-direction. The maximum deflection has shifted towards one end owing to the multiple point constraint.

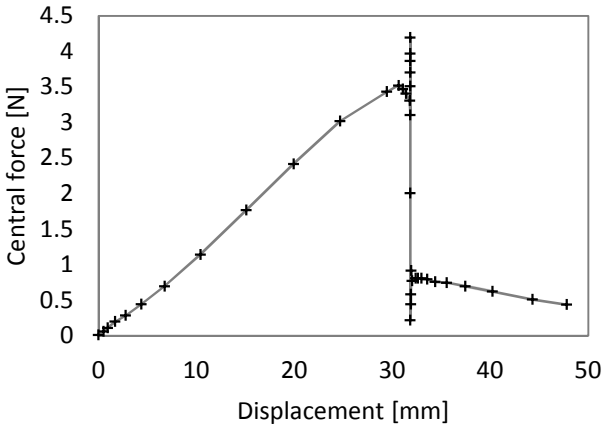

Figure 11 - Central force versus displacement for a compression rate of 0.1% for a stiffener thickness of 3mm.

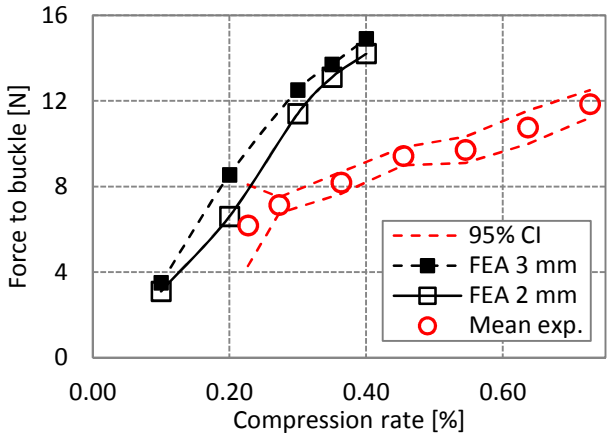

Figure 12 - Comparison of reaction forces to buckle when external load was applied. Experimental data represent the mean of three loadings for each value of strain apart from 0.55% for which there are four data. Confidence intervals indicate the range of values that one can be 95% confident contains the true mean values based on repeated measures.

Figure 12 compares the force required to buckle the diaphragm. The experimental and FEA data are well matched up to a spine compression rate of 0.2% but can be seen to diverge after this. The relationship between the force to induce buckling and the compression rate is approximately linear for both the FEA results. The numerical simulations give a force per unit compression rate of about 36 N/%. In contrast, the force to buckle and compression rate found experimentally is lower (10 N/%). This is discussed further in Section 5.

4.3 Investigation into the stiffness

Figure 13 shows how the transverse deflection and the radius of curvature of spine change as the spine compression rate increases. The transverse deflection, *h*, increases with spine compression parabolically up to a compression rate of 0.4%. This corresponds to the point at which the spine curvature begins to level off, as shown in Figure 13(b). As expected, the radius of curvature decreased with increasing compression rate.

The effect of stiffener thickness on the maximum transverse deflection and on the radius of curvature is also shown in Figure 13, in which data for a 2 mm and a 3 mm thick stiffener are plotted. The radius of curvature of spine is reduced when a thicker stiffener is used due to the longitudinal stretching of the stiffeners. The transverse deflection is slightly higher with the more flexible stiffener.

5 Discussion

Physical experiments and finite element analysis of a scale model of part of the SeaWave WEC have been used to demonstrate the longitudinal and transverse bending of the device under compressive force. The results are compared with those of the authors' earlier work [10] in which a first order mathematical theory was developed to predict the bending of the spine and the diaphragm. The work in this paper showed that the transverse deflection, *h*, increased with increasing strain (compressive force) and with increasing side stiffener thickness, and the longitudinal curvature, *R*, decreased with increasing strain (compressive force) and side stiffener thickness. The force to bend the deformed model, the snap-through force, also increased with increased strain.

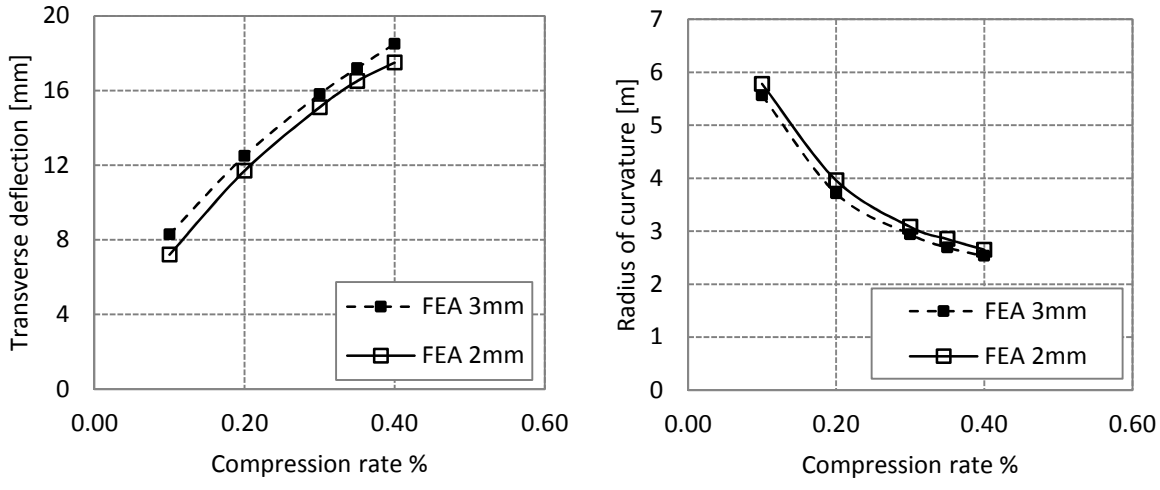

(a) (b)

Figure 13 - Effect of stiffener modulus on the (a) spine radius of curvature and (b) transverse deflection.

5.1 Validation of the numerical model

The physical model experiments were used as a comparison and a validation of the FEA model for both curvature and snap-through force experiments, Figure 7 and Figure 12. There was some divergence between the physical and the FEA results.

The FEA overestimated the transverse deflection (and underestimated the longitudinal radius of curvature) compared to that measured on the physical model. This indicates that the FEA model was stiffer than the physical model. This can be attributed to the edge conditions of the diaphragm and to the model having been created from one solid part. First, the diaphragm was created from one solid body in order to save the computation costs. This added an extra longitudinal bending stiffness even though this was mitigated by using a small Young's modulus in the longitudinal direction.

Secondly, the FEA model did not allow wrinkling of the stiffeners due to the in-plane bending because the stiffeners were idealised as one body. In reality, the stiffeners were punched and bolted, which facilitated wrinkling as observed in physical tests. Therefore the transverse deflection, h, was overestimated due to the overestimation of the stiffener stiffness. As a consequence, the longitudinal radius of curvature of spine was smaller in FEA modelling than measured in the physical model. As indicated by the theory, there is a trade-off between h and R. The theoretical results of both transverse deflection and longitudinal radius of curvature are closer to the physical results, owing to the fitting parameter, α, which was included in the theoretical model. The FEA model did not require the fitting parameter but tended to overestimate the stiffness of the structure.

Figure 7 indicated that there was a residual value on the physical model for both h and R. This can be attributed to two sources: deformation under self-weight and plastic deformation of the whole structure. The additional mass at either end of the structure due to the steel end-plates and the low torsional stiffness of the undeformed structure meant that the model was susceptible to lateral-torsional buckling under self-weight. In addition, owing to the way in which the model was constructed with the ends bolted to two steel end-plates, Figure 3, the model was only able to deform in one direction along the x-axis. Repeated use of the model, and its inherent hysteresis, caused the residual curvature as shown in Figure 7, in which the mean value of up to 6 data is plotted. It is likely that increasing the compression past a certain threshold (discussed further below) caused the permanent deformation of the components.

5.1.1 Uncertainty in the measurements

Repeated measurements of the loading and unloading of the spine allowed uncertainty surrounding the true value of the transverse deflection to be mitigated. The 95% confidence intervals indicate the range in which we can be 95% sure the mean values lie. However, if the value of residual transverse curvature on the spine increased over time, one could not assume that repeated measures would reduce the effects of random error as the error would be systematic and possibly increasing. It is not likely that the residual value of the transverse curvature would continue to increase and so it seems sensible to assume an asymptote may be reached.

A further source of uncertainty in the measure of the model deformation, though not accounted for in Figure 7, is the value of the compressive force applied. The strain measurement was based on the number of turns of the compression bolt and it was sometimes difficult to determine when the bolt had contacted the end of the spine in the polycarbonate end piece, particularly as the model did not return to fully flat. Uncertainty in the compression value would be an initial uncertainty of, at maximum, one turn of the bolt, which equates to a compression rate of less than 0.05%. After that, it was possible to get accuracy of ±5 degrees on each turn, which equates to an uncertainty of ±6e-4% between subsequent measurements on a loading cycle. For the unloading it was noticed that values of deflection were sometimes higher at the same value of compression for the preceding loading cycle. This is most likely due to friction in the system but a lack of paired loading/unloading cycles does not allow further investigation or quantification of this phenomenon.

Confidence intervals are not shown for the longitudinal curvature in Figure 7(b) since the values shown are the result of only one experiment. Instead, the error bars indicate the upper and lower values for R given the accuracy to which the distances could be measured (D and H in Figure 4). These upper and lower bounds are small compared to the differences between the experimental values and the theoretical or FEA results.

5.1.2 Deviation at high strain values

The transverse deflection of the model, shown in Figure 7(a), followed the theoretical values closely up to a compression rate of 0.40%. After this there was a down turn in the transverse deflection as the compression value increased. In this zone, the confidence intervals were much wider than before owing to fewer experimental measurements being made: the results in Figure 7(a) are typically the mean of four data from compression rates of 0.57% onwards. Despite the wide confidence intervals that may indicate a plateau rather than a drop in transverse deflection with increased compression, this trend was seen on all loading cycles that reached this point.

The decrease in transverse deflection is likely to be associated with the change to higher buckling modes: the midpoint longitudinally would be the location of highest transverse curvature in mode one buckling but would have zero curvature in mode two buckling. If this is the case and the curve continues at the same rate, the compression rate needed to induce buckling mode two could be estimated as falling between 0.70% and 0.80%.

5.2 Effect of spine compression

The experimental results indicated that there was a delay between the loading of the structure and the onset of buckling. This is related to initial stretching of the stiffeners, which were only 0.75 mm thick. During the assembly process, the stiffeners wrinkled when they were bolted around the rest of the model layers and as a result, the onset of the buckling of the whole structure is obscured. The measurements in loading and unloading were averaged to minimise the error. The difference between the experimental measurement and the analyses increases above compression rates of 0.45%, Figure 7. Both the FEA and theoretical simulation results show that the transverse deflection continues to increase while the spine radius of curvature is almost constant. This did not happen in the experimental measurement. The structure became stiffer due to the widening of the central cavity which was not captured by the FEA model and the theoretical analysis. Nevertheless a good agreement is obtained between the experiments and the finite element analysis in the lower values of compression rate.

5.3 Effect of stiffener material

Figure 13 showed how the thickness of the stiffener increased the transverse curvature and decreased the radius of longitudinal curvature at a given compression rate. With thicker stiffeners at the edges of the device, there is more resistance to the compression in the spine and a tighter longitudinal curvature is expected (reduced R). This may only make a small difference; the radius of curvature, R, for the 3 mm stiffener is between 94% and 96% of that for the 2 mm stiffener. However, since the energy stored in the device is inversely proportional to the square of the radius [10], with all other parameters being the same, this difference would allow 13% more energy to be stored in the device with a thicker stiffener.

The transverse deflection is altered by a similar amount proportionally with the move to a thicker stiffener, albeit in the opposite direction and the bending of the structure transversely is another way in which energy is stored in the system. The transverse curvature has a pronounced effect on the overall stiffness of the structure as the central cavity opens up and as mass is concentrated away from the centre line, the structure becomes stiffer.

5.4 Response to external load and energy capture potential

Whilst the experiments described in the paper did not include all the elements of a SeaWave WEC, for example the hose was omitted, we can use the results to infer energy storage and hence performance of the device as a WEC. The stored energy in the structure can be calculated by integrating the force-displacement curve shown in Figure 11. For example, with a compression rate 0.1%, the stored energy will be approximately 0.5 J/m when the buckling occurs. For the full-scale device, designed to have a diameter of 1 m, this stored energy should be 12.5 J/m. The total stored energy for the proposed 1000 m long structure will be 25000 J. It is inferred that 12500 J will be captured and released when the whole structure undergoes one cycle of buckling. If we assume that under wave loading the buckle takes 5 s to travel through the device, the power is equivalent to 5 kW. The theory presented in previous work [10] shows that the energy stored in the structure is inversely proportional to the square of the longitudinal radius, meaning that for a tighter longitudinal curve, more energy would be stored in the structure.

The energy stored is a function of both the compression and the force to induce the snap-through behaviour, which is related to the stiffness of the structure. The compression of a bistable buckled beam was investigated by Cazottes *et al.* [23] in terms of the forces required to actuated the beams as switches. They found that increasing the pre-compression could force the beam to buckle in a higher order mode, which reduced the actuation force necessary. During the experiments and simulations reported in this paper, only the first buckling mode was used but in a full-scale SeaWave device that is several hundred metres long, higher order buckling would be used. For given spine characteristics, higher order buckling implies a higher pre-compression, which may be linked to higher CAPEX costs as materials and structures have to withstand larger forces. However, the trade-off is that the device would need lower wave-induced actuation forces to switch between states and therefore would be responsive to a larger range of wave forces. This is still speculative at this stage since the functioning of the device under the action of waves that have very different lengths compared to the buckled length of the device is unknown.

6 Conclusions

In summary, the simplified theory predicted the trend in transverse deflection and the longitudinal curvature of the structure. This forms a good basis for optimisation of the structure in terms of structural design and material selection. However, it requires a fitting parameter to account for the effect of edge condition of the diaphragm. The FEA model can predict the behaviour of the structure without the need of a fitting parameter while the structure is subject to spine compression or external load. It allows for the prediction of longitudinal curvature, the transverse deflection due to spine compression and the critical load to buckle the curved structure. Although the FEA model generally overestimates the longitudinal bending stiffness of the structure owing to the complex behaviour of the thin shell stiffeners, it provides a tool to estimate the upper bound of energy storage capacity. This is a major step in the design of the wave energy converter proposed.

The FEA model of the response of the structure to external central load shows when the structure will buckle. This provides a method to evaluate the potential of the structure to store energy. A case study based on a spine compression of 0.1% shows that the work needed to buckle the structure

is about 0.5 J/m, equivalent to 25 kJ for a 1 m diameter, 1000 m long full-size structure or 5 kW for a period of 5 s wave. It was speculated that buckling in a higher mode could decrease the snap-through buckling force necessary, at the expense of a larger initial spine compression. Whilst the existing FEA model is unable to model this behaviour, future iterations of the theoretical model or the physical model could test this hypothesis.

7 Acknowledgements

KMC gratefully acknowledges the support from HEFCE funding for the overall research and the grant from Santander Scholarships for the building of the physical models. MM was funded by the School Engineering (formerly the School of Marine Science and Engineering) at Plymouth University through a PhD studentship. Constructive discussion with Professor Long-yuan Li is also acknowledged.

8 References

1. Carbon Trust, *The potential for cost reduction - insights from the Carbon Trust Marine Energy Accelerator*, in Accelerating marine energy. 2011
2. López, I., J. Andreu, S. Ceballos, I. Martínez de Alegría, and I. Kortabarria, *Review of wave energy technologies and the necessary power-equipment.* Renewable and Sustainable Energy Reviews, 2013. **27**: p. 413-434.
3. Holmes, B., *Tank Testing of Wave Energy Conversion Systems*. Marine Renewable Energy Guides. 2009, London: BSI.
4. Etnier, S.A., *Twisting and bending of biological beams: Distribution of biological beams in a stiffness mechanospace.* Biological Bulletin, 2003. **205**(1): p. 36-46.
5. Shan, Y., M. Philen, A. Lotfi, S. Li, C.E. Bakis, C.D. Rahn, and K.W. Wang, *Variable Stiffness Structures Utilizing Fluidic Flexible Matrix Composites.* Journal of Intelligent Material Systems and Structures, 2009. **20**(4): p. 443-456.
6. Boriek, A.M. and J.R. Rodarte, *Effects of transverse fiber stiffness and central tendon on displacement and shape of a simple diaphragm model.* Journal of Applied Physiology, 1997. **82**(5): p. 1626-1636.
7. Kelly, D.A., *The Functional Morphology of Penile Erection: Tissue Designs for Increasing and Maintaining Stiffness.* Integrative and Comparative Biology, 2002. **42**(2): p. 216-221.
8. Kier, W.M., *The diversity of hydrostatic skeletons.* The Journal of Experimental Biology, 2012. **215**(8): p. 1247-1257.
9. Collins, K.M., O. David-West, H. Le, and D.G. Greaves, *From concept to laboratory testing: the development cycle of a novel wave energy converter*, in *International Conference on Ocean Energy*. 2014: Halifax, NS.
10. Le, H.R., K.M. Collins, D.M. Greaves, and N.W. Bellamy, *Mechanics and materials in the design of a buckling diaphragm wave energy converter.* Materials & Design, 2015. **79**(0): p. 86-93.
11. Crosby, A.J., *Why should we care about buckling?* Soft Matter, 2010. **6**(22): p. 5660-5660.
12. Hu, N. and R. Burgueño, *Buckling-induced smart applications: recent advances and trends.* Smart Materials and Structures, 2015. **24**(6): p. 063001.
13. Qiu, J., J.H. Lang, and A.H. Slocum, *A curved-beam bistable mechanism.* Journal of Microelectromechanical Systems, 2004. **13**(2): p. 137-146.
14. Zhao, J., J.Y. Jia, X.P. He, and H.X. Wang, *Post-buckling and snap-through behavior of inclined slender beams.* Journal of Applied Mechanics-Transactions of the Asme, 2008. **75**(4).
15. Deshpande, S., *Buckling and post buckling of structural components*. 2010, University of Texas at Arlington.
16. Li, S.R. and Y.H. Zhou, *Post-buckling of a hinged-fixed beam under uniformly distributed follower forces.* Mechanics Research Communications, 2005. **32**(4): p. 359-367.
17. Camescasse, B., A. Fernandes, and J. Pouget, *Bistable buckled beam: Elastica modeling and analysis of static actuation.* International Journal of Solids and Structures, 2013. **50**(19): p. 2881-2893.
18. Casals-Terre, J. and A. Shkel. *Dynamic analysis of a snap-action micromechanism*. in *Sensors, 2004. Proceedings of IEEE*. 2004.
19. Fang, W. and J.A. Wickert, *Post Buckling of Micromachined Beams.* Journal of Micromechanics and Microengineering, 1994. **4**(3): p. 116-122.
20. Chai, H., *On the post-buckling behavior of bilaterally constrained plates.* International Journal of Solids and Structures, 2002. **39**(11): p. 2911-2926.
21. Hao, G. and J. Mullins, *On the infinitely-stable rotational mechanism using the off-axis rotation of a bistable translational mechanism.* Mech. Sci., 2015. **6**(1): p. 75-80.
22. Vangbo, M., *An analytical analysis of a compressed bistable buckled beam.* Sensors and Actuators a-Physical, 1998. **69**(3): p. 212-216.
23. Cazottes, P., A. Fernandes, J. Pouget, and M. Hafez, *Bistable Buckled Beam: Modeling of Actuating Force and Experimental Validations.* Journal of Mechanical Design, 2009. **131**(10): p. 101001-101001.
24. Galchev, T., H. Kim, and K. Najafi, *Micro Power Generator for Harvesting Low-Frequency and Nonperiodic Vibrations.* Journal of Microelectromechanical Systems, 2011. **20**(4): p. 852-866.
25. Lajnef, N., R. Burgueño, W. Borchani, and Y. Sun, *A concept for energy harvesting from quasi-static structural deformations through axially loaded bilaterally constrained columns with multiple bifurcation points.* Smart Materials and Structures, 2014. **23**(5): p. 055005.
26. Gi-Woo, K. and K. Jaehwan, *Compliant bistable mechanism for low frequency vibration energy harvester inspired by auditory hair bundle structures.* Smart Materials and Structures, 2013. **22**(1): p. 014005.
27. Ashby, M.F., *Materials selection in mechanical design*. 3rd ed. 2005, Amsterdam ; Boston: Butterworth-Heinemann. xiv, 603 p.
28. ABAQUS, *ABAQUS reference manual.* 2015.